Supplement of Earth Surf. Dynam., 10, 1253–1272, 2022
https://doi.org/10.5194/esurf-10-1253-2022-supplement

Supplement of

A combined approach of experimental and numerical modeling for 3D hydraulic features of a step-pool unit

Chendi Zhang et al.

Correspondence to: Chendi Zhang (chendinorthwest@163.com and zhangchendi@igsnrr.ac.cn) and Mengzhen Xu (mzxu@mail.tsinghua.edu.cn)

S1: Model verification

Two methods were used to verify the hybrid model: (i) the grid independence test; and (ii) the comparison between simulated and experimental results.

A series of simulations under the discharge of 43.6 L/s were used to test the grid convergence, with various mesh sizes but identical settings of computational domain (transverse range of Y = -24.5 to 24.5 cm) and boundary conditions. We tested six mesh sizes, i.e., 0.50 cm, 0.375 cm, 0.30 cm, 0.27 cm, 0.25 cm and 0.24 cm, and the corresponding cell numbers of the main mesh block which covered the step-pool unit were 0.89 million, 2.11 million, 4.12 million, 5.61 million, 7.15 million, and 8.08 million. The comparison of water surface at the middle section, Y = 0.3 cm, is exhibited in Fig. S1 and the distributions of flow velocity at this section are shown in Fig. S2. The variations of both the water surface and flow velocity distribution become insignificant after the mesh size is reduced to below 0.3 cm. This result illustrates that the grid size of 0.25 cm which was finally chosen for all the simulations in this study satisfies the requirement of grid independence.

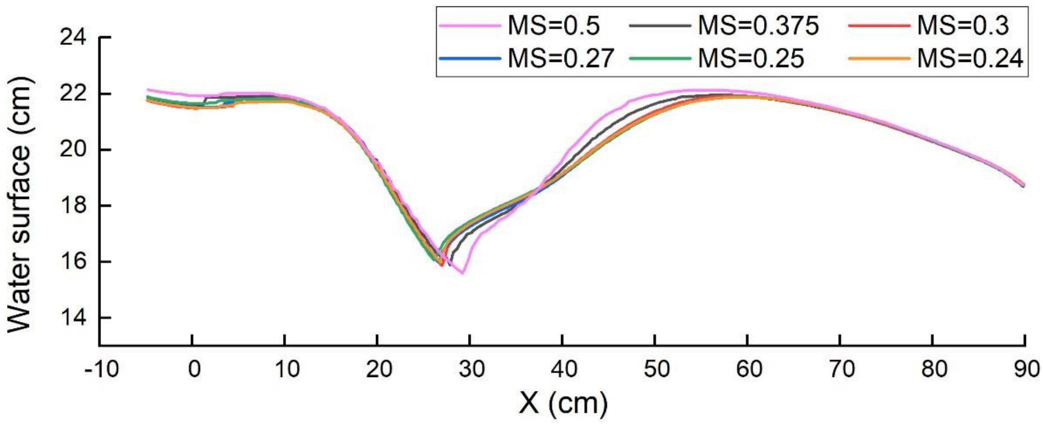

Figure S1: Water surface profiles of the simulations with different mesh sizes at the discharge of 43.6 L/s at the middle longitudinal section at Y = 0.3 cm. MS is short for mesh size. The flow direction is from left to right in each plot.

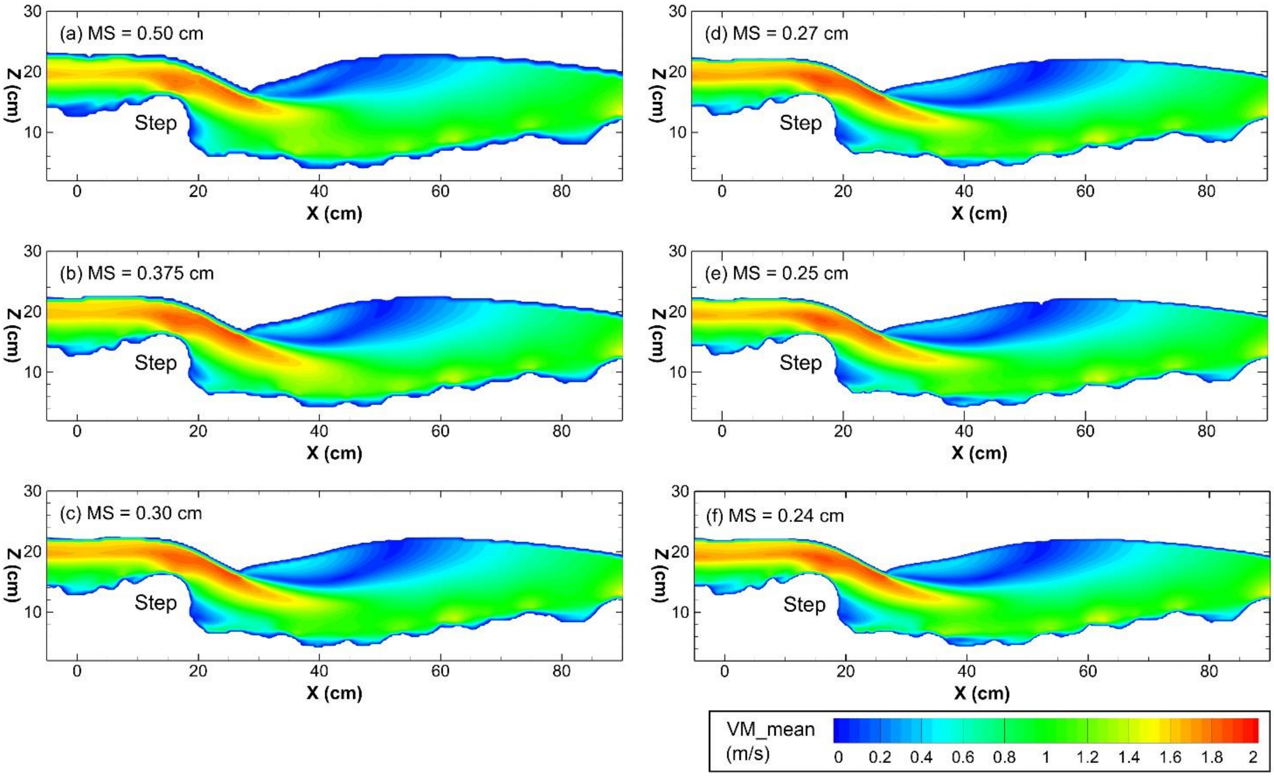

Figure S2: Contours of velocity magnitude in the longitudinal section at Y = 0 cm under the flow condition with the discharge of 43.6 L/s at different mesh sizes (MSs): (a) 0.50 cm; (b) 0.375 cm; (c) 0.30 cm; (d) 0.27 cm; (e) 0.25 cm; (f) 0.24 cm. The flow direction is from left to right.

Two measurements in the previous flume experiments (Zhang et al., 2018, 2020) were used to validate the numerical models: (i) longitudinal water surface profiles extracted from the side cameras (Fig. S3a); and (ii) water surface features recorded in pictures by the top camera (Fig. S3b). All the image frames taken by the side camera and top camera were calibrated according to the tape measures stuck to the side walls and the constant flume width respectively. Both the water surface from the side view and the upstream edge of the recirculation cell at the water surface from the top view were depicted by polylines in each calibrated image frame. The polylines of all the 30 image frames that were captured over 60 s were rasterized by 0.5 cm gridding. Then the max, 75% quantile, mean, 25% quantile and min of the water surface elevations at each streamwise location or the upstream edge of the recirculation cell at the water surface at a transverse location for all the image frames were calculated and used to compare with the time-averaged values obtained from the CFD simulations.

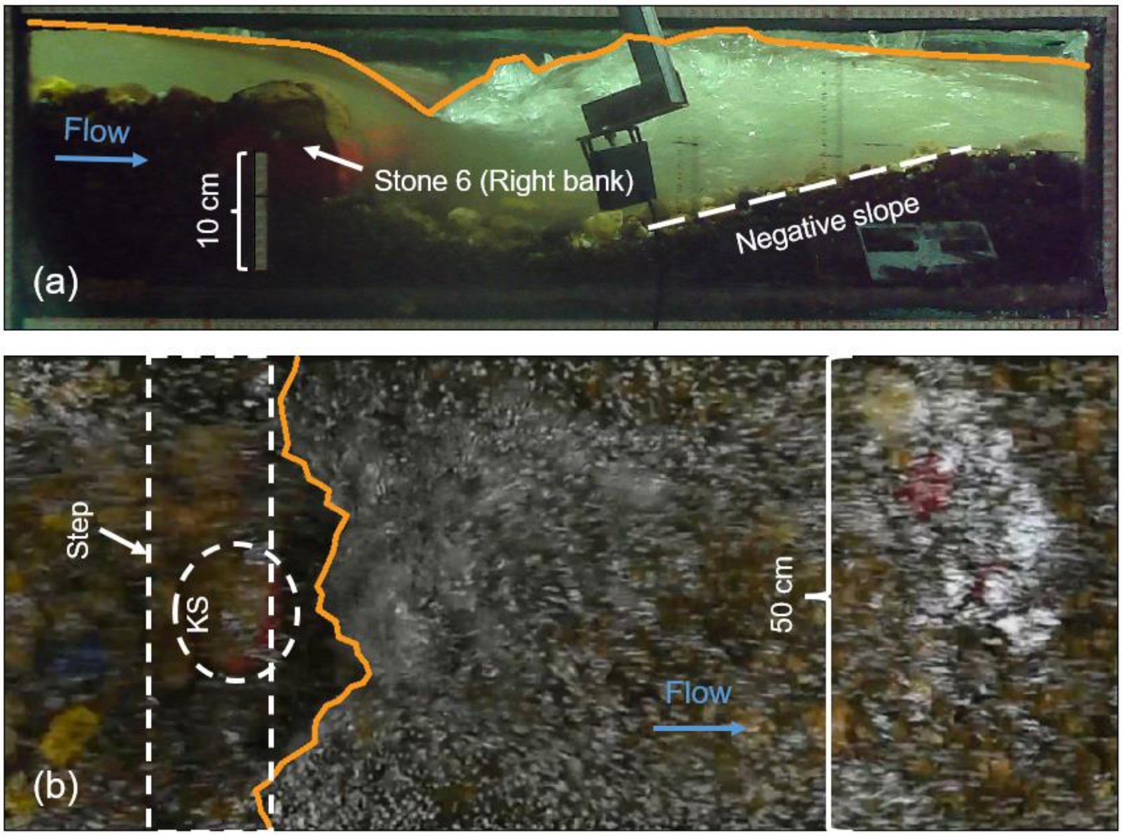

Figure S3: Measurements of water surfaces (orange lines) used in model verification: (a) water surface profiles from both sides of the flume; (b) upstream edge of the recirculation cell at the water surface from the top view. KS refers to keystone in figure (b).

Figures S4-S6 demonstrate the comparisons of water surface between the experimental measurements and simulated results at the flow rate of 32.1, 43.6, and 49.9 L/s at both sides of the flume. The comparisons illustrate that the simulated water surface profiles are generally comparable with the experimental measurements, even at the highest flow condition tested in the experiment with fluctuating water surface. The simulated water surfaces upstream and downstream of the hydraulic jump in the pool match well with the measurements. However, clear deviations of the simulations from the measured water surfaces appear at the recirculation cell near the water surface where intense air entrainment occurs. The air entrainment was not considered in the CFD model in order to reduce model complexity and the requirement for computation resources. This simplification might neglect the volume expansion of the fluids at the flow recirculation cell of the hydraulic jump and hence, underestimate the elevation of the free water surface.

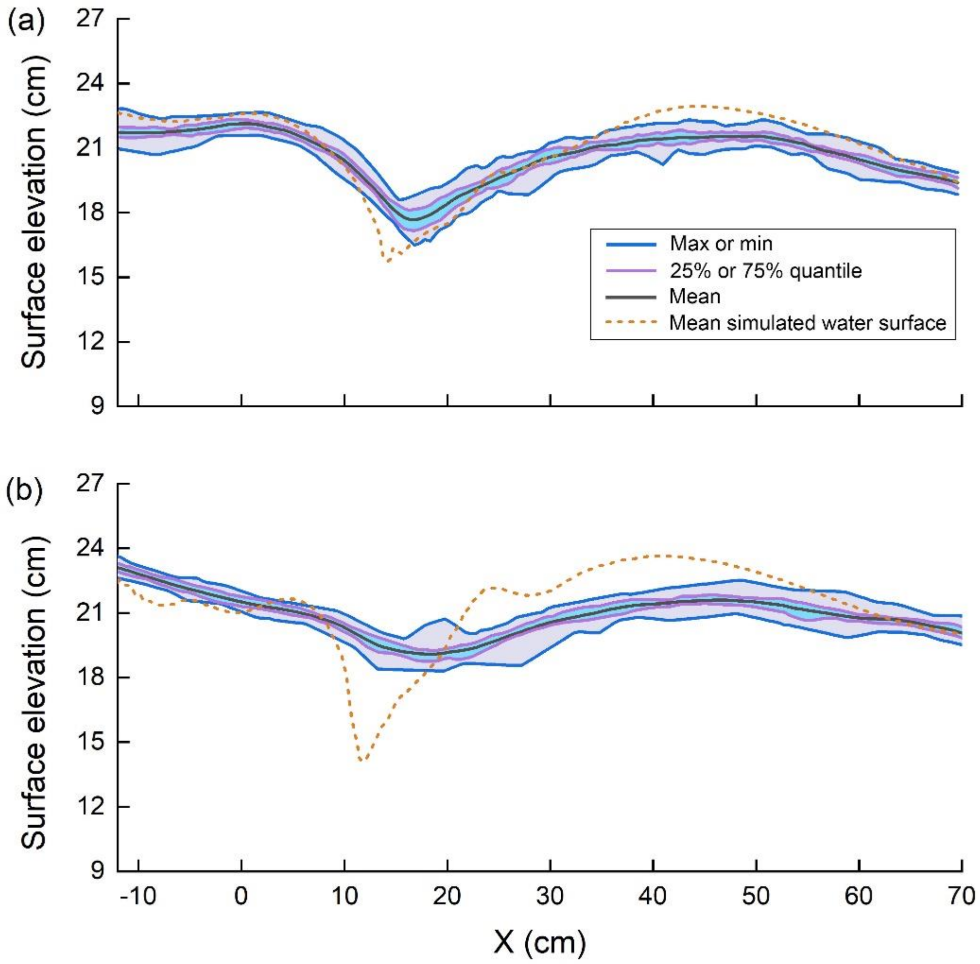

Figure S4: Comparison of water surface between the measurement and simulation under the discharge of 32.1 L/s at (a) left side, and (b) right side of the flume. The max, 75% quantile, mean, 25% quantile and min of the measured water surfaces are presented in solid lines. The flow goes from left to right in each plot.

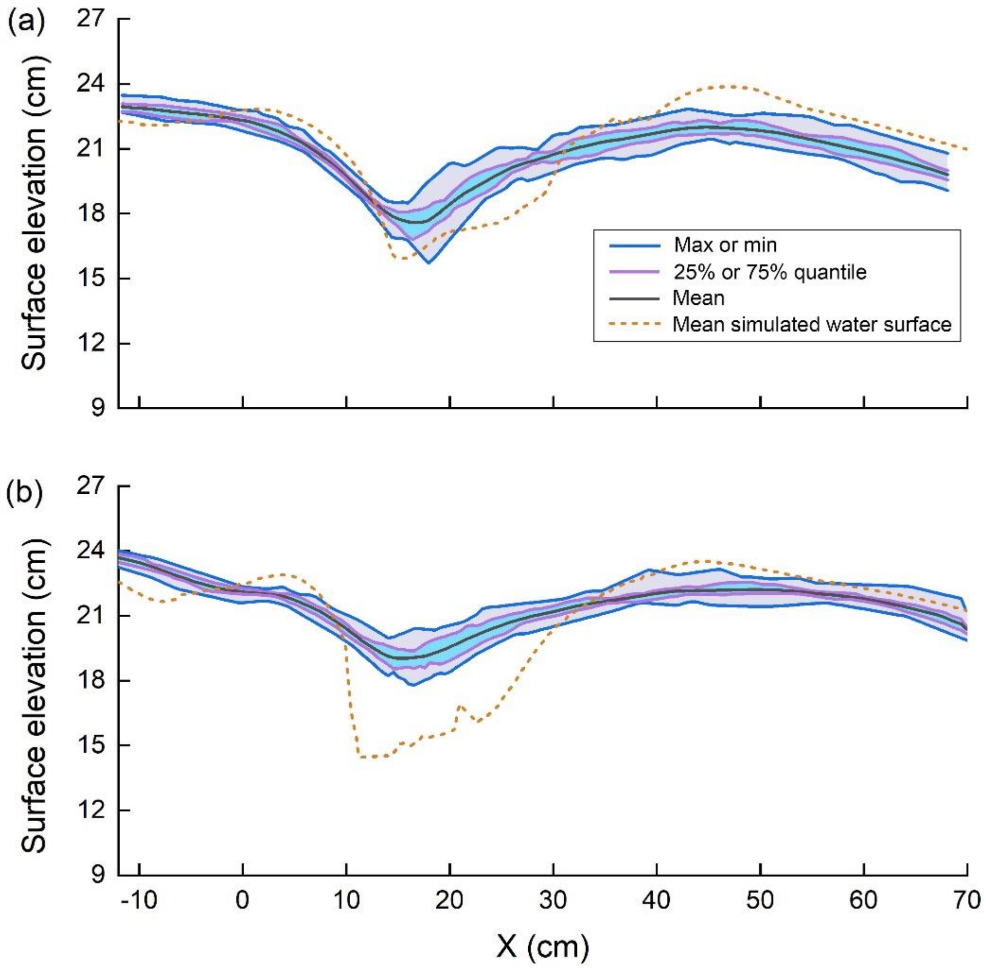

Figure S5: Comparison of water surface between the measurement and simulation under the discharge of 43.6 L/s at (a) left side, and (b) right side of the flume. The max, 75% quantile, mean, 25% quantile and min of the measured water surfaces are presented in solid lines. The flow goes from left to right in each plot.

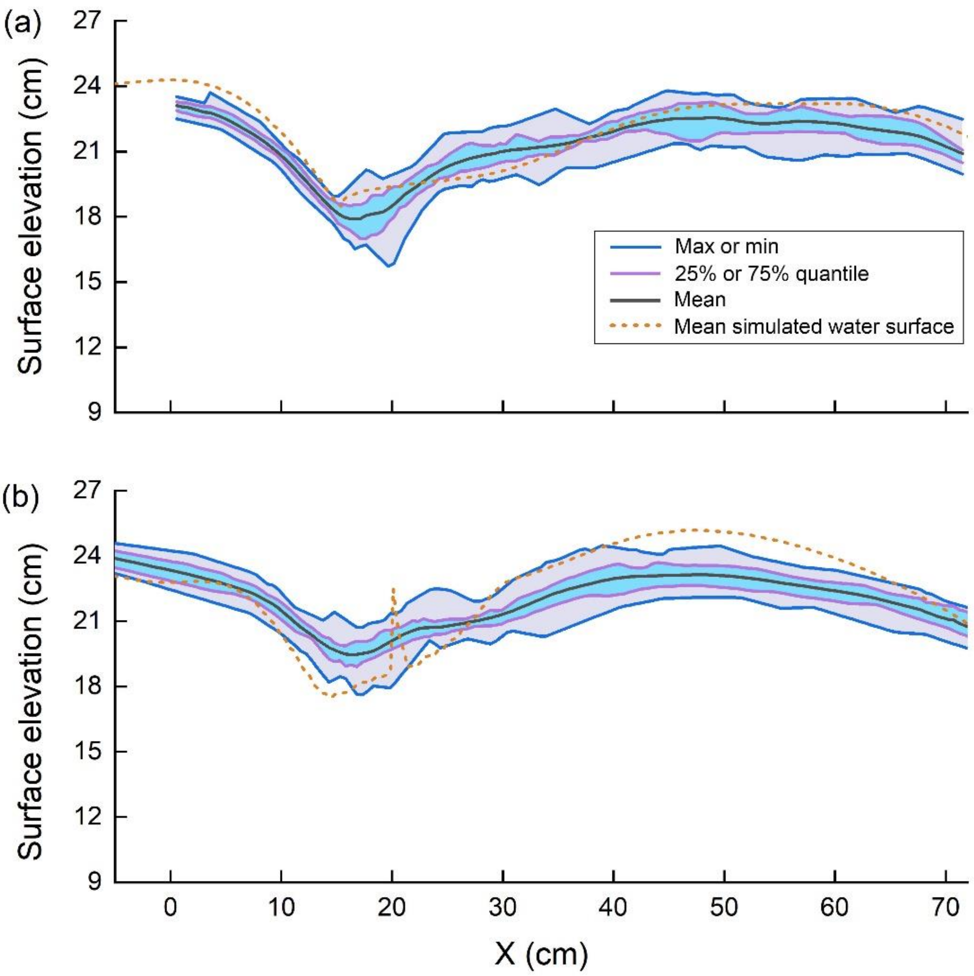

Figure S6: Comparison of water surface between the measurement and simulation under the discharge of 49.9 L/s at (a) left side, and (b) right side of the flume. The max, 75% quantile, mean, 25% quantile and min of the measured water surfaces are presented in solid lines. The flow goes from left to right in each plot.

Figure S7 and Table S1 exhibit the validation of the upstream boundary of the flow recirculation cell near the water surface from the top view. All the boundaries were extracted manually for the experimental and numerical results, based on the distinct contrast of flow velocity in the jet separated from the step surface and the recirculation cell near the water surface (Fig. S3b). The simulated boundary is generally located in the range of measured boundaries (Fig. S7) and the deviations of the simulation under all the tested discharges are acceptable (Table S1). These results further verify the feasibility of the combined approach to simulate the complex surface flow features over a step-pool unit. Both the comparisons from sideview and top view show that the combined approach succeeded in capturing the flow characteristics for a step-pool feature built in the physical experiment.

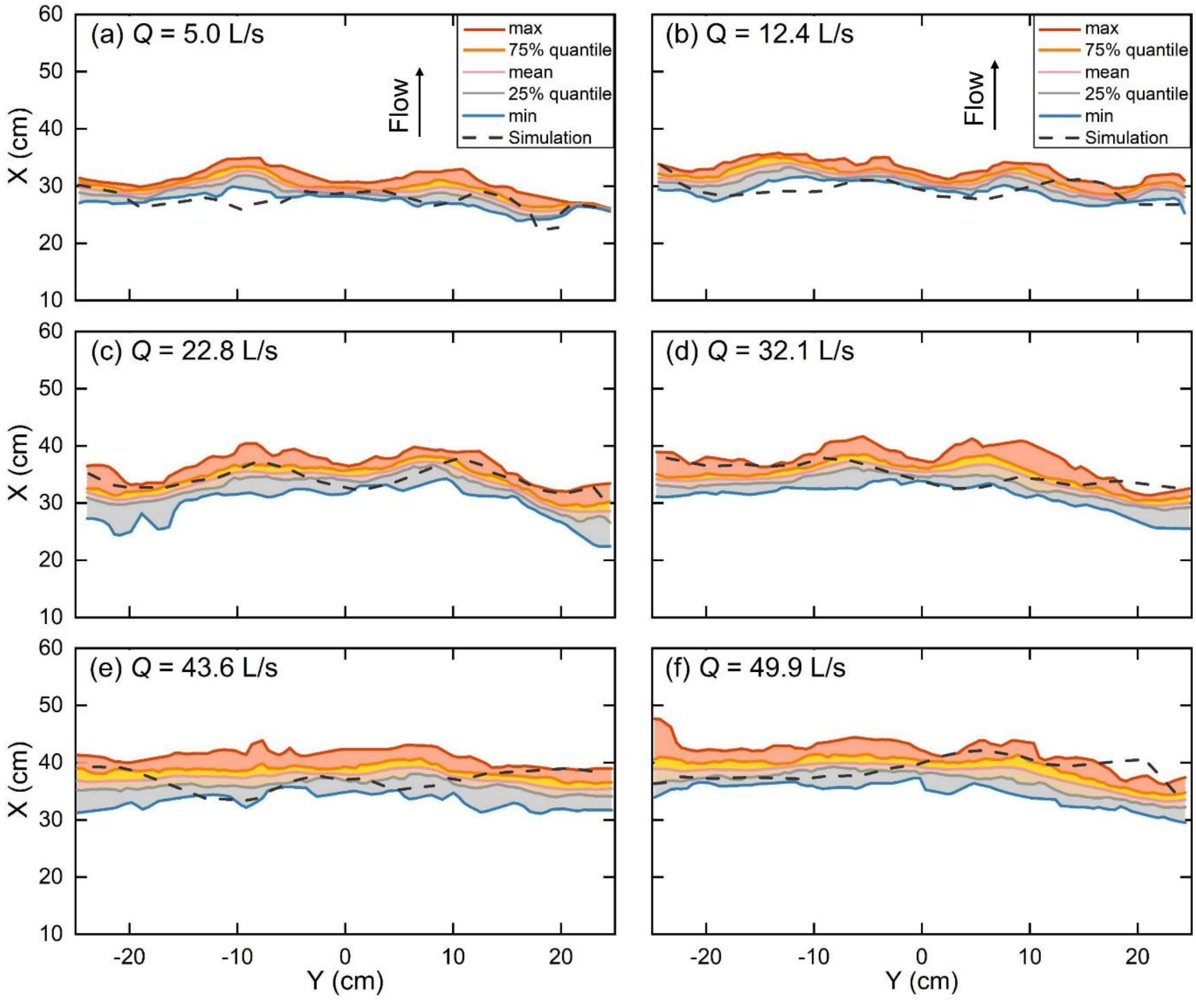

c

Figure S7: The extracted upstream boundaries of the flow recirculation cell near the water surface from simulated results (in dots) and experimental measurements at all the tested discharges. The max, 75% quantile, mean, 25% quantile and min X values of the measured boundaries are presented in solid lines while the mean simulated boundaries are plotted in dashed lines.

Table S1: Error indices for the simulated upstream boundaries of the flow recirculation cells associated with the jump regime from the top view

Q (L/s)	*ME* (cm)	*MAE* (cm)	*MSE* (cm)	*RMSE* (cm)	*SDE* (cm)
5	1.54	1.71	5.71	2.39	0.99
12.4	1.82	2.40	7.16	2.68	0.73
22.8	-0.76	1.75	3.90	1.97	1.66
32.1	-0.71	2.02	5.44	2.33	2.11
43.6	0.46	2.21	6.28	2.51	2.42
49.9	-0.92	2.45	8.13	2.85	2.54

S2: Supplemental figures for flow properties and forces

Figure S8 presents the longitudinal distribution of Froude number in section Y=0. Figures S9-S14 provide supplementary information on flow properties and flow forces at the discharges of 5.0, 12.4, 22.8 and 32.1 L/s.

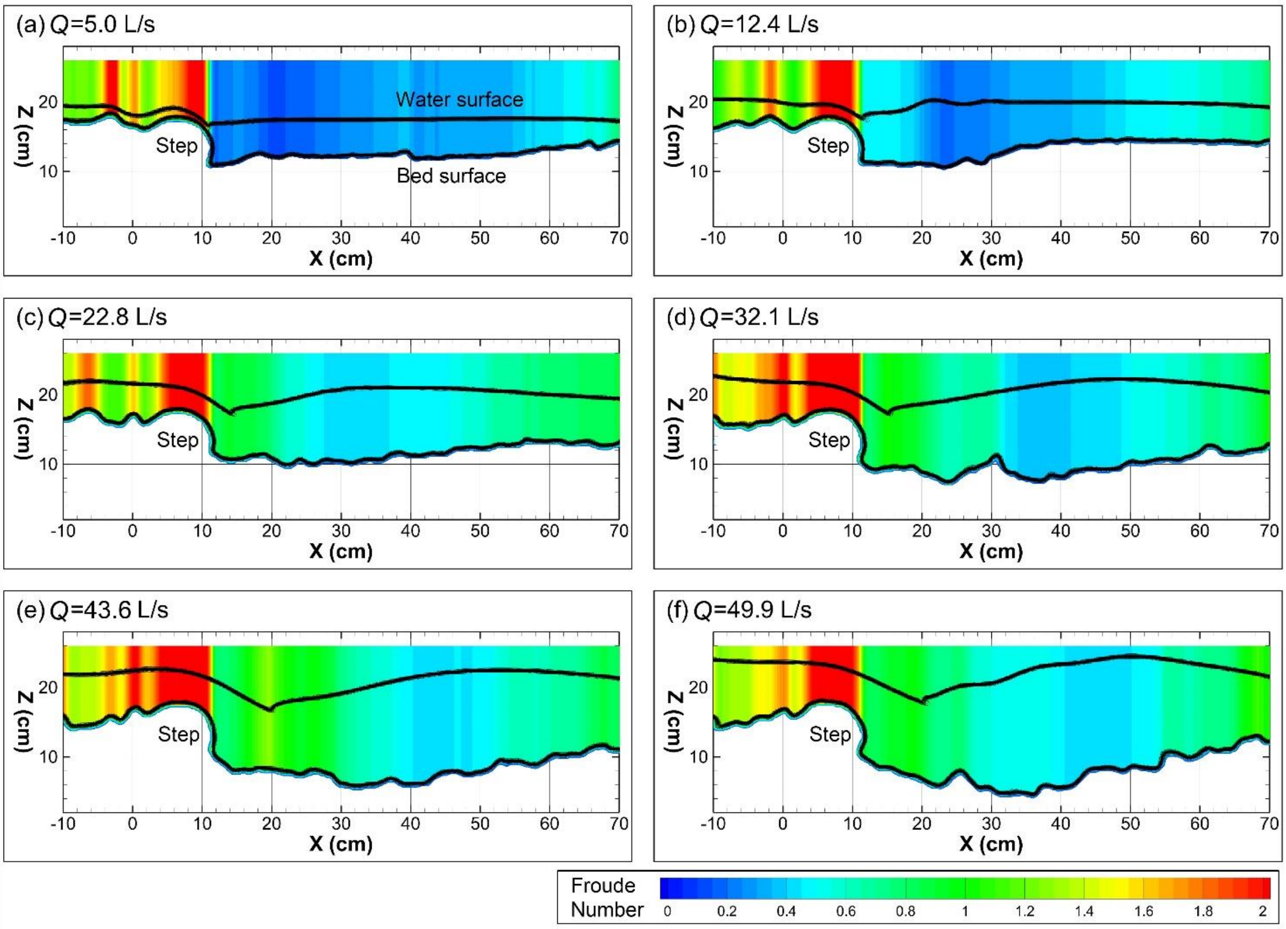

Figure S8: Distribution of time-averaged Froude number in the longitudinal section Y = 0 cm for all flow rates. The flow goes from left to right.

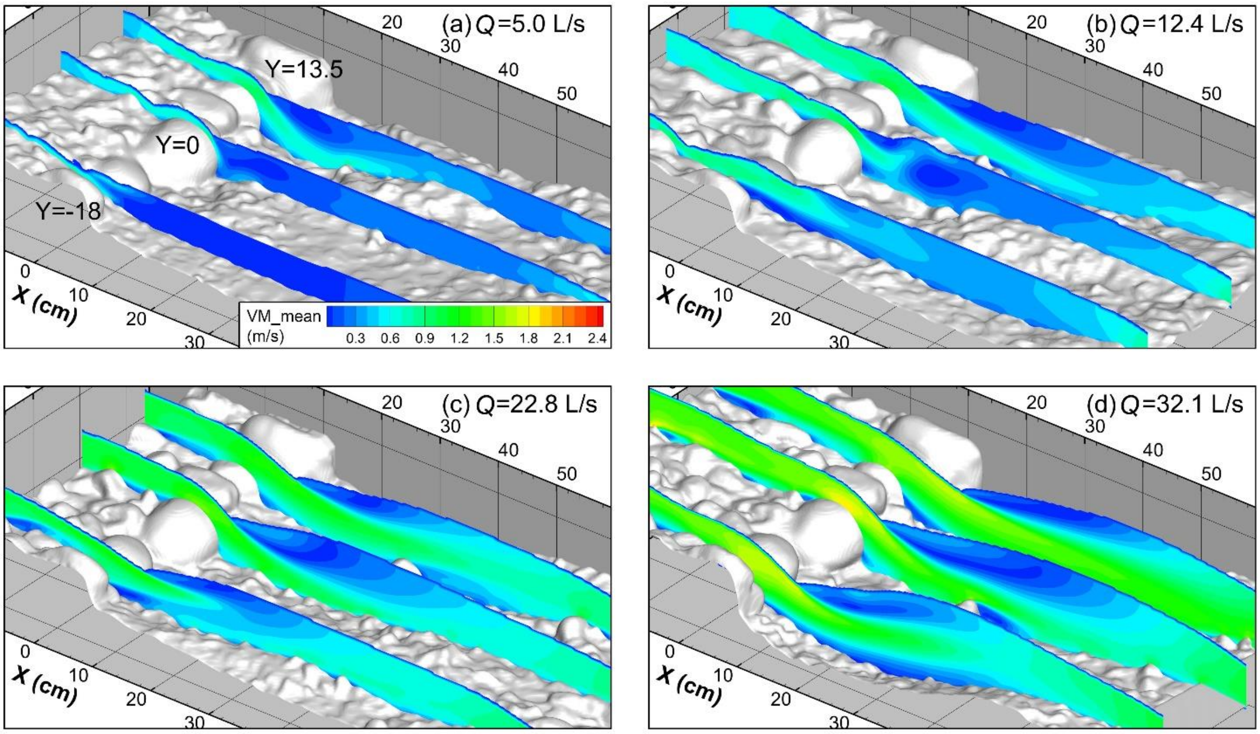

Figure S9: Distribution of time-averaged velocity magnitude (VM_mean) in three longitudinal sections (Y = -18, 0 and 13.5 cm, marked in figure (a)). The spacings for X, Y, and Z axes are all 10 cm in the plots.

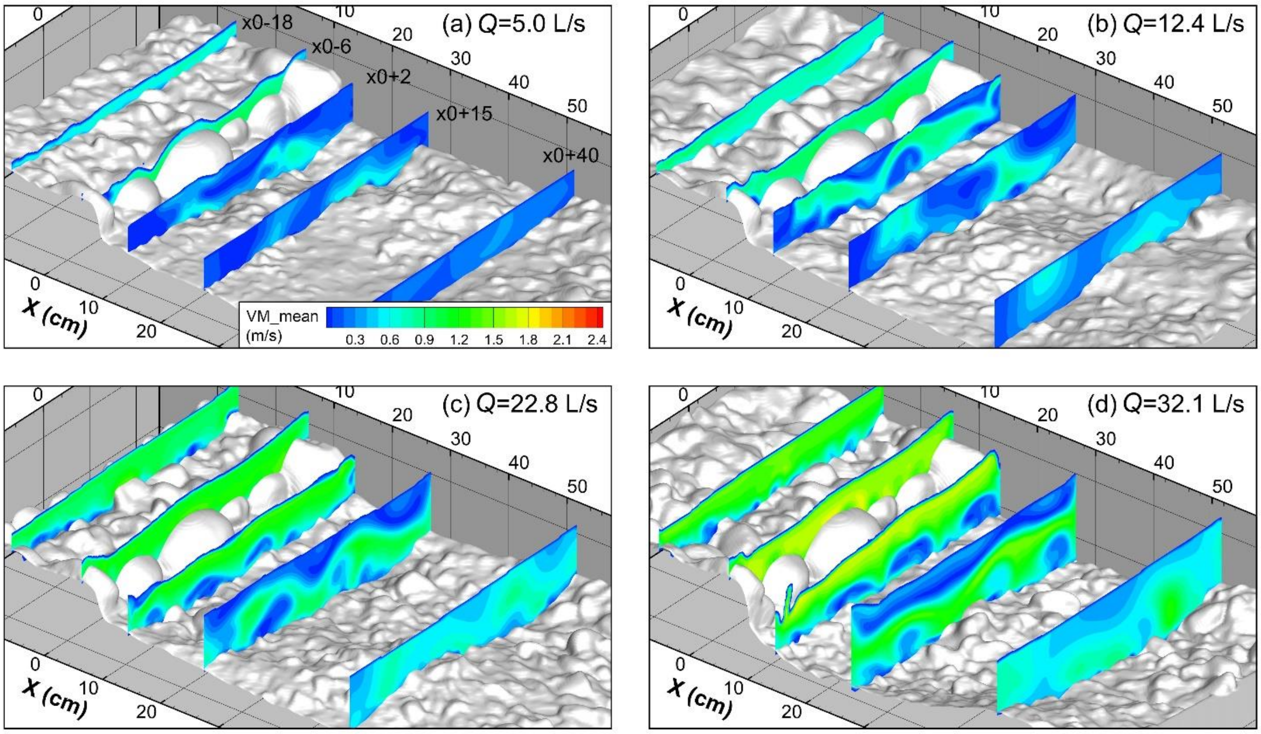

Figure S10: Distribution of time-averaged flow velocity at five cross sections relative to the reference cross section x0. The reference cross section x0 is located at the downstream end of the keystone (KS). The five sections are marked in panel (a). The spacings for X, Y, and Z axes are all 10 cm in the plots.

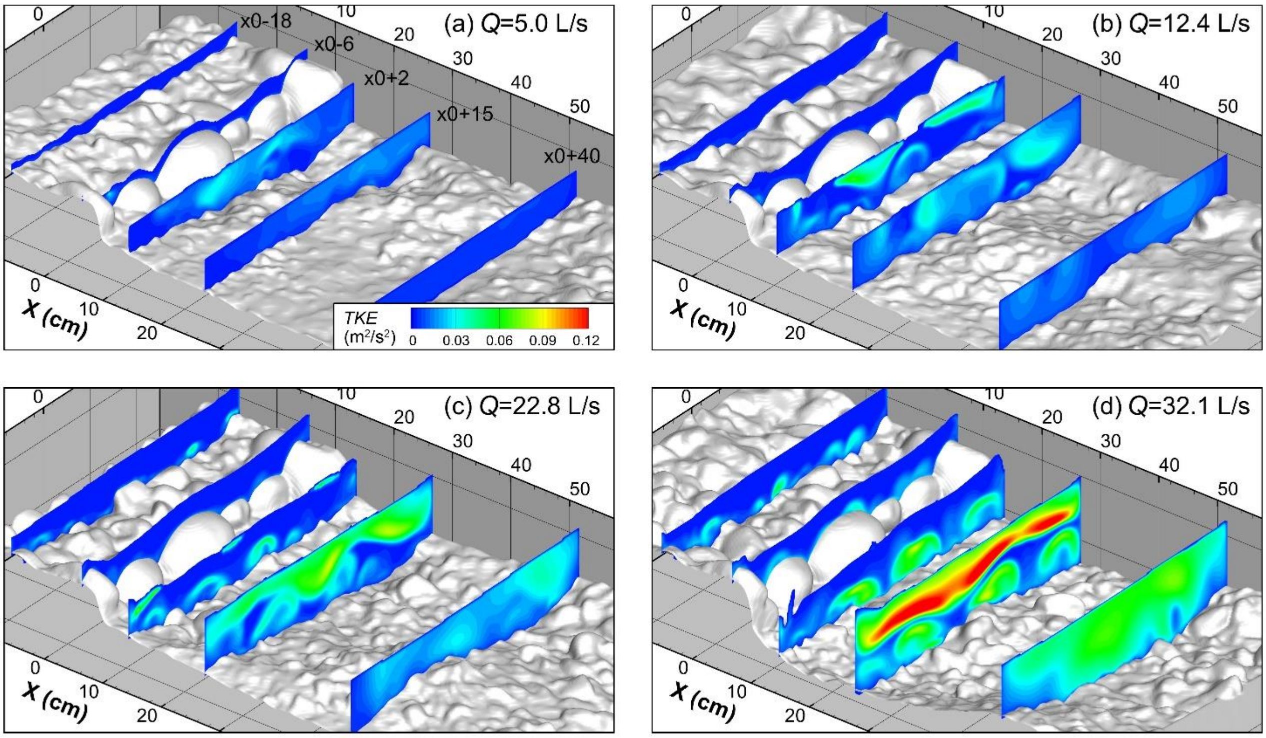

Figure S11: Distribution of the time-averaged turbulence kinetic energy (*TKE*) in the five cross sections described in Fig. S10. The spacings for X, Y, and Z axes are all 10 cm in the plots.

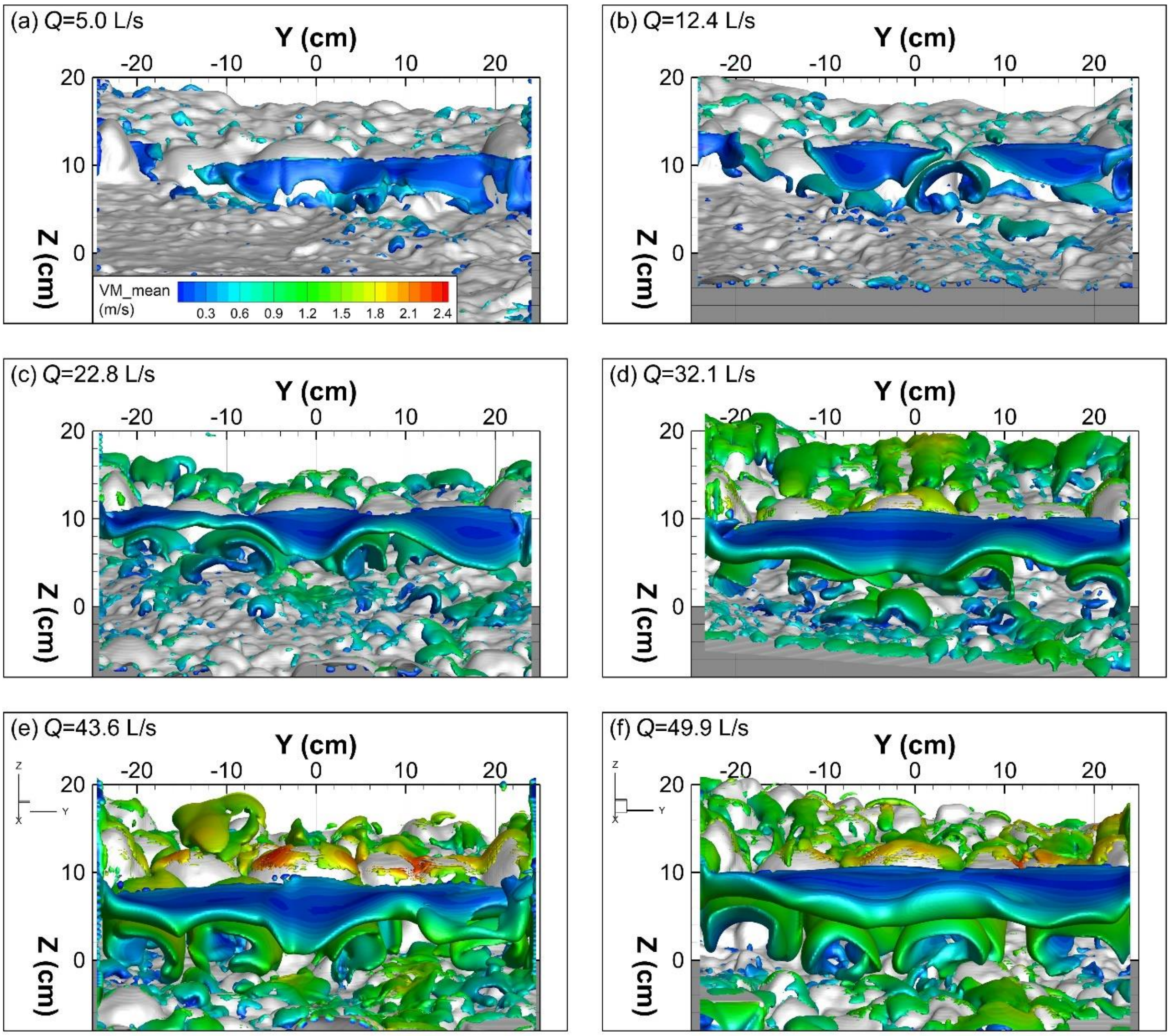

Figure S12: Instantaneous flow structures extracted using the *Q*-criterion ($Q_{criterion}$=1200) and colored by the magnitude of flow velocity. This figure plots the same coherent structures as Fig. 7 but in a different view.

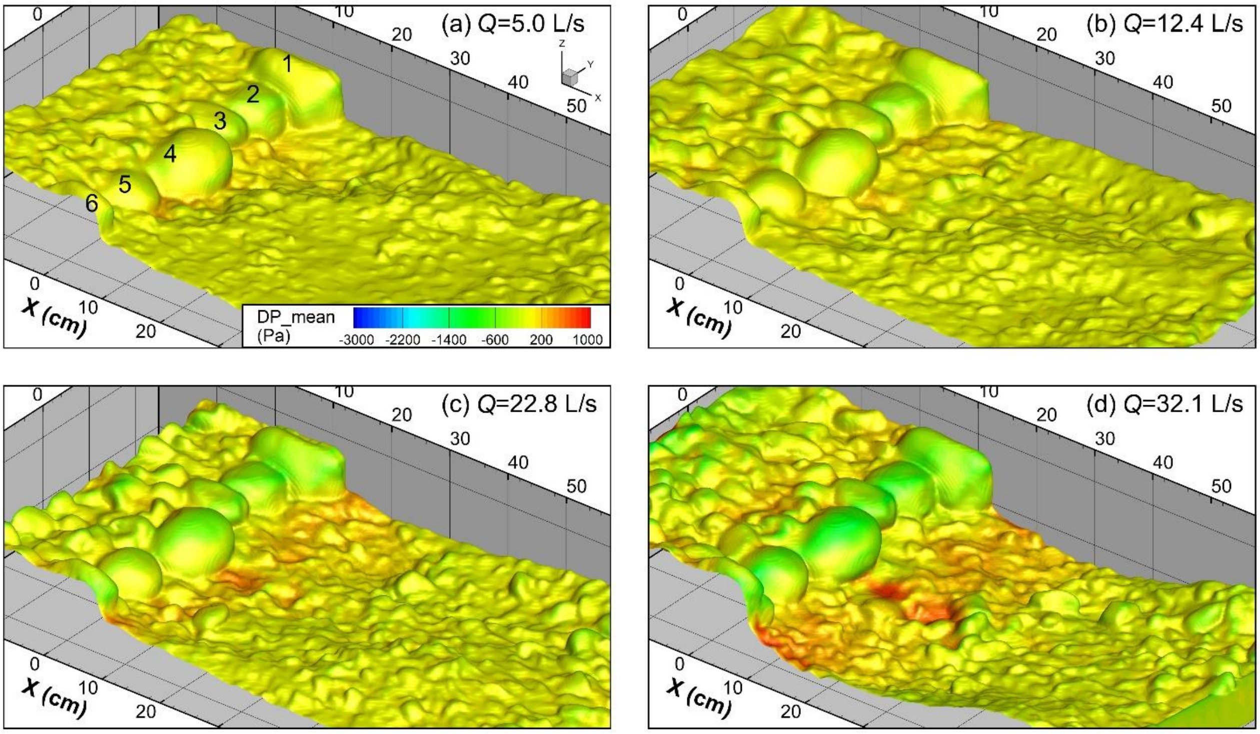

Figure S13: Distributions of time-averaged dynamic pressure (DP_mean) on the bed surface of the step-pool unit under four flow rates. The numbers of step stones are marked in all the plots. The negative values in the plots result from the setting of standard atmospheric pressure = 0 Pa, whose absolute value is 1.013×10^5 Pa.

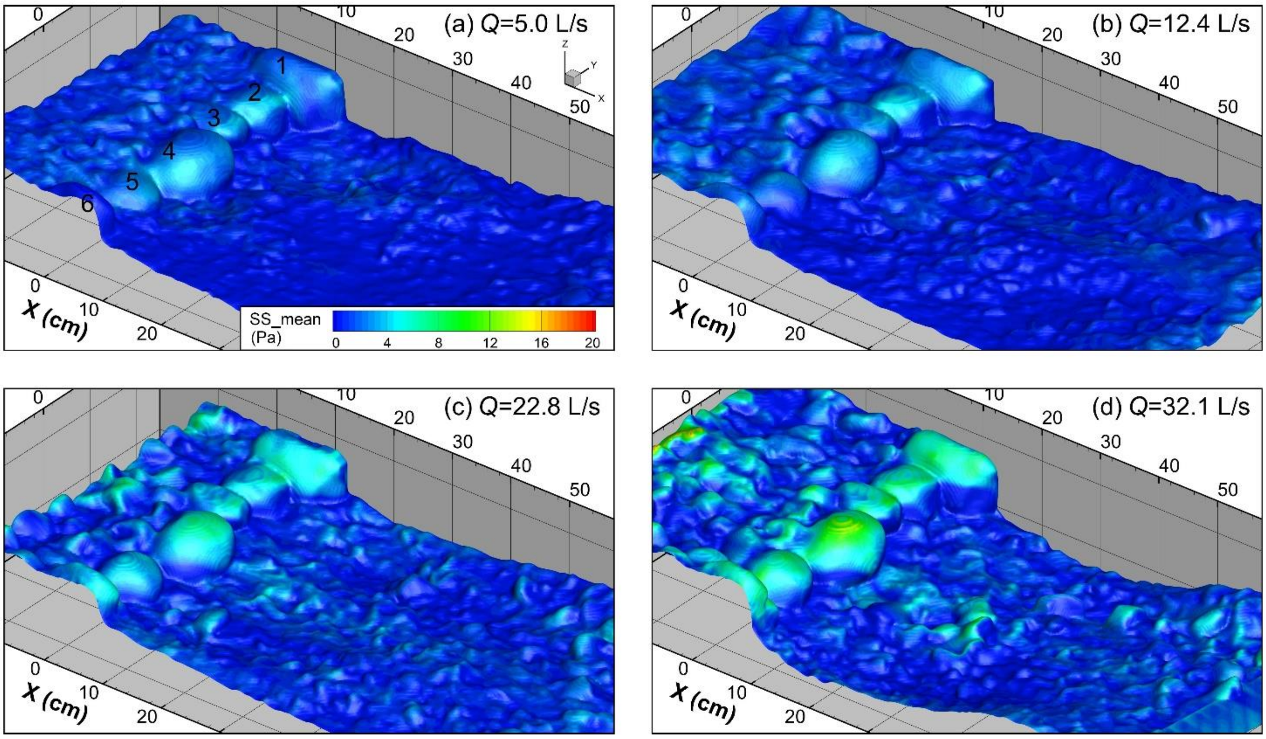

Figure S14: Distributions of time-averaged shear stress (SS_mean) on the bed surface of the step-pool unit under four flow rates. The numbers of step stones are marked in all the plots. The standard atmospheric pressure is set as 0 Pa.

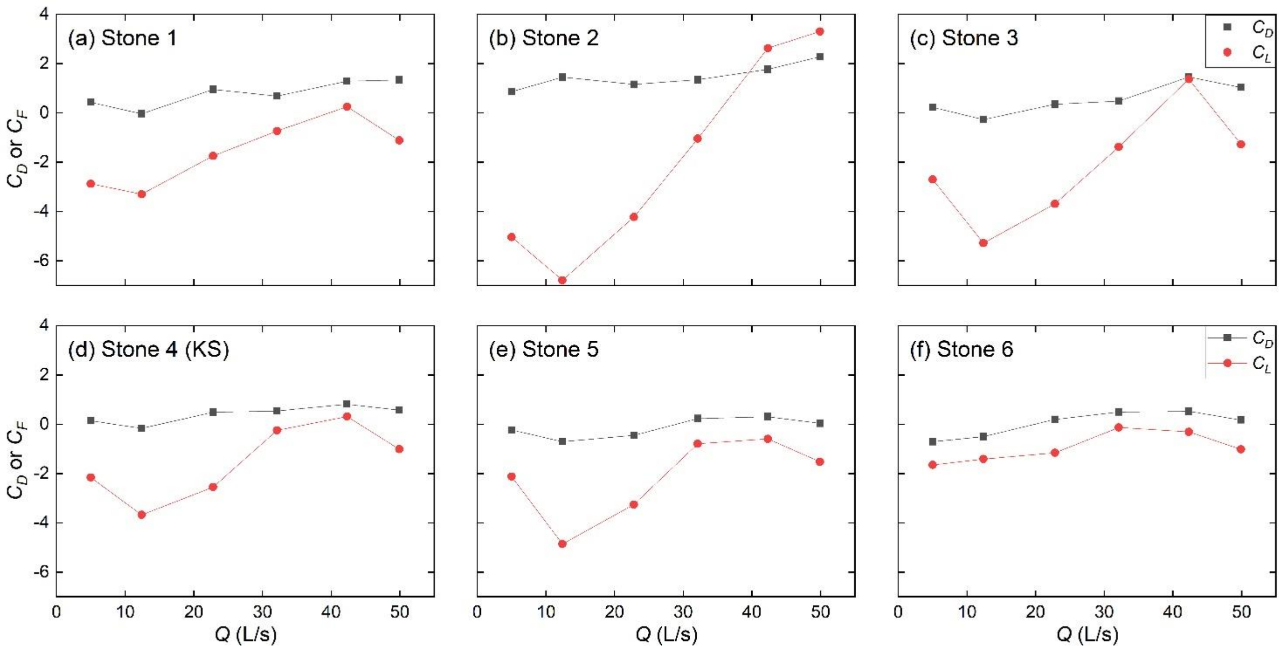

Figure S15: Variation of drag (C_D) and lift (C_L) coefficient of the step stones along with flow rate. Stone numbers are consistent with those in Fig. S14. KS is short for keystone. The negative values of C_D correspond to the drag forces towards the upstream while the negative values of C_L correspond to the lift forces pointing downwards.

S3: Influence of micro-bedforms in the pool on surrounding hydraulics

To illustrate the effect of the micro-bedforms as grain clusters on the surrounding hydraulics, we take the scenario at Q = 49.9 L/s as an instance, shown in Fig. S16-17. The four vortices attached to the step toe show intact configurations in the cross section at x0+8, which is located upstream of all the micro-bedforms in the pool and hence, is used as a reference section. When a protruding grain/cluster is located within a vortex attached to the step, it has almost no disturbance on the flow field or *TKE* nearby (e.g., G1 and G3 in Fig. S16c to d and Fig. S17b to c). In contrast, if a cluster is located in the gap between two vortices (e.g., G2 and G4 in Fig. S16c to d and Fig. S17b to c), both the flow velocity and *TKE* increase near the cluster but the increase is limited in a thin layer (with thickness < 1 cm) above the grain surface. These results suggest that the grain clusters have very limited influence on the surrounding hydraulics at the pool bottom, where the alternation of high-speed flows and vortices formed at the step toe dominates the flow structures near the bed surface. The interference of the grain clusters at the pool bottom on local hydraulics keeps being suppressed during the development of pool scour. In contrast, the grain clusters on the negative slope increase the flow velocity and turbulence above them, and the affected area is greatly expanded compared with those at the pool bottom (Fig. S16e and S17d).

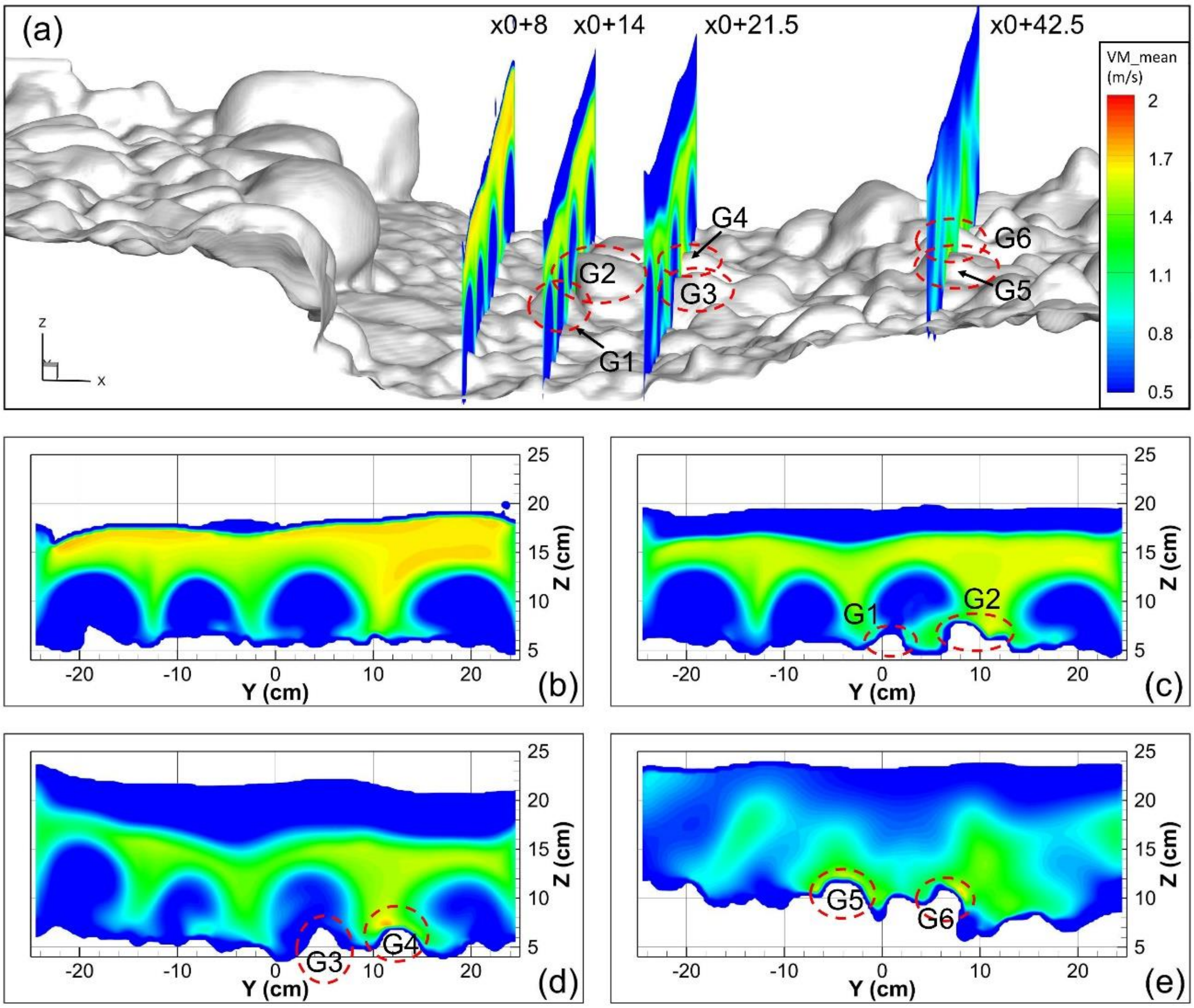

Figure S16. Figure (a) shows the locations of the cross sections and target coarse grains at *Q* = 49.9 L/s. Figures (b) to (e) show the distribution of velocity magnitude (VM_mean) in the four chosen cross sections: (a) x0+8.0; (b) x0+14.0; (c) x0+21.5; (d) x0+42.5. The number in each index of the cross section refers to the downstream distance from the reference section (unit: cm). G1 to G6 refer to 6 protruding grains in the micro-bedforms in the pool.

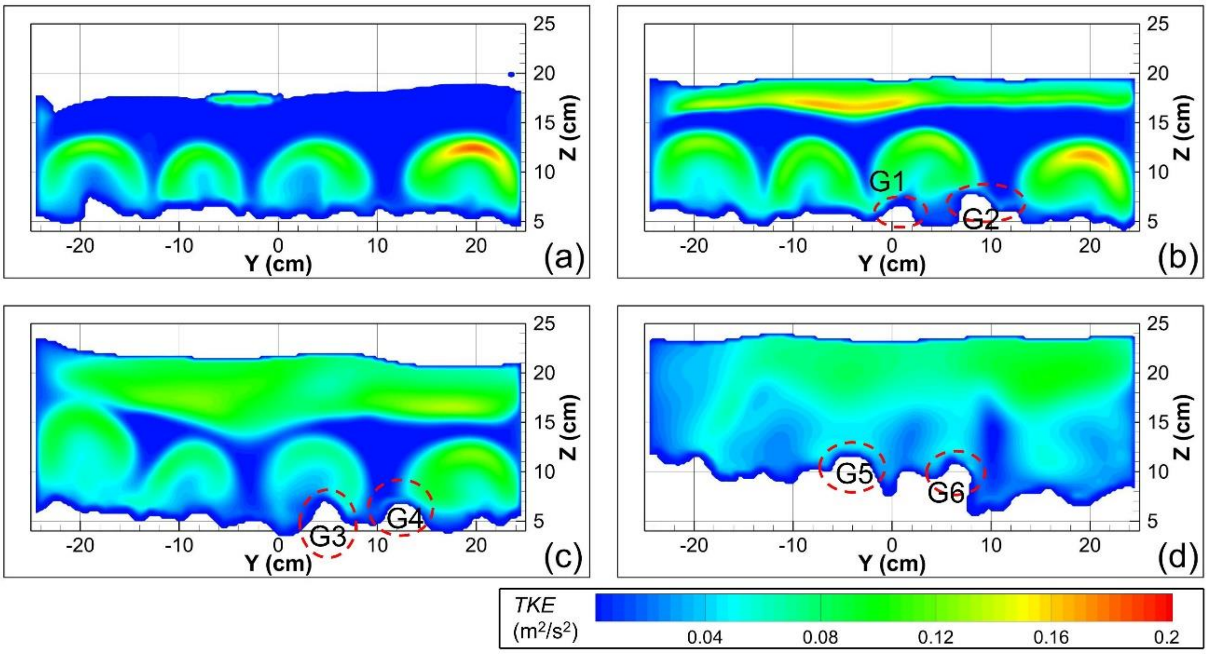

Figure S17. The distribution of turbulent kinetic energy (*TKE*) in the same cross sections as in figure S16: (a) x0+8.0; (b) x0+14.0; (c) x0+21.5; (d) x0+42.5.

References

Zhang, C., Xu, M., Hassan, M. A., Chartrand, S. M., and Wang, Z.: Experimental study on the stability and failure of individual step-pool, Geomorphology, 311, 51-62, https://doi.org/10.1016/j.geomorph.2018.03.023, 2018.

Zhang, C., Xu, M., Hassan, M. A., Chartrand, S. M., Wang, Z., and Ma, Z.: Experiment on morphological and hydraulic adjustments of step-pool unit to flow increase, Earth Surf. Proc. Land., 45(2), 280-294, https://doi.org/10.1002/esp.4722, 2020.